Long-term relative decline in evapotranspiration with increasing runoff on fractional land surfaces

Ren Wang[1,2,3], Pierre Gentine[4,5], Jiabo Yin[6], Lijuan Chen[1,2], Jianyao Chen[7,8], and Longhui Li[1,2,3]

[1]Key Laboratory of Virtual Geographical Environment (Nanjing Normal University), Ministry of Education, Nanjing, 210023, China

[2]School of Geographical Sciences, Nanjing Normal University, Nanjing, 210023, China

[3]Jiangsu Center for Collaborative Innovation in Geographical Information Resource Development and Application, Nanjing, 210023, China

[4]Earth and Environmental Engineering Department, Columbia University, New York, NY 10027, USA

[5]Earth Institute, Columbia University, New York, NY 10025, USA

[6]State Key Laboratory of Water Resources and Hydropower Engineering Science, Wuhan University, Wuhan, 430072, China

[7]School of Geography and Planning, Sun Yat-sen University, Guangzhou, 510275, China

[8]Guandong Key Laboratory for Urbanization and Geo-simulation, Sun Yat-sen University, Guangzhou, 510275, China

Correspondence to: Ren Wang (wangr67@mail2.sysu.edu.cn) or Pierre Gentine (pg2328@columbia.edu)

Abstract. Evapotranspiration (ET) accompanied by water and heat transport in the hydrological cycle is a key component in regulating surface aridity. Existing studies documenting changes in surface aridity have typically estimated ET using semi-empirical equations or parameterizations of land surface processes, which are based on the assumption that the parameters in the equation are stationary. However, plant physiological effects and its responses to a changing environment are dynamically modifying ET, thereby challenging this assumption and limiting the estimation of long-term ET. In this study, the latent heat flux (ET in energy units) and sensible heat flux were retrieved for recent decades on a global scale using machine learning approach and driven by ground observations from flux towers and weather stations. This study resulted in several findings, that is, the evaporative fraction (EF)—the ratio of latent heat flux to available surface energy—exhibited a relatively decreasing trend on fractional land surfaces; in particular, the decrease in EF was accompanied by an increase in long-term runoff as assessed by precipitation (P) minus ET, accounting for 27.06% of the global land areas. The signs are indicative of reduced surface conductance, which further emphasizes that land surface vegetation has major impacts in regulating water and energy cycles, as well as aridity variability.

1 Introduction

Evapotranspiration (ET) mainly includes two processes: (1) evaporation from soil and plant surfaces and (2) transpiration from plants to the atmosphere (Miralles et al., 2020). These processes connect the transfer of moisture and energy in soil, vegetation, and atmospheric systems (Salvucci et al., 2013; Yang et al., 2020). Quantifying changes in the exchange of moisture and heat between the land and atmosphere is very important for understanding and characterizing water and energy cycles, which has implications in various fields such as hydrology, climatology, and agronomy (Hoek van Dijke et al., 2020; Gentine et al., 2016; Komatsu and Kume, 2020).

ET is expected to intensify with the warming climate, thereby contributing to the increase in surface aridity stress (Baruga et al., 2020; Berg et al., 2016; Fu et al., 2014; Trenberth et al., 2014). However, quantification of changes in aridity/wetness is usually derived from traditional drought indices such as the Standardized Precipitation Evapotranspiration Index (Vicente-Serrano et al., 2015), which is embedded with a semi-empirical equation, such as the Thornthwaite equation or Penman–Monteith equation, for ET estimation (Dai et al., 2013; Sheffield et al., 2012). Using potential evaporation rather than actual ET or calculating offline ET using meteorological variables from climate model outputs in traditional drought indices, the calculation implicitly assumes that soil can always supply moisture to meet the atmospheric evaporation demand, which is an incorrect assumption for most land surfaces (Greve et al., 2014; Milly and Dunn, 2016; Yang et al., 2020). Moreover, when using a semi-empirical equation for ET estimation, some parameters such as soil surface resistance and stomatal resistance, are assumed to be stationary over time; however, we know that these parameters are dynamically changing with environmental conditions (Miralles et al., 2011; Yang et al., 2019; Zhou et al., 2016).

Why are the soil surface resistance and stomatal resistance not stationary? Changes in plant stomata and leaf area, with increasing CO_2 concentrations in particular, reshape the allocation of surface energy fluxes and affect plant transpiration (Forzieri et al., 2020; Sorokin et al., 2017; Mallick et al., 2016; Williams and Torn, 2015). With increasing CO_2 concentrations, the density and opening degree of leaf stomata decrease, while the water-use efficiency and biomass production of plant increase, which can modify vegetation transpiration and even affect soil moisture or surface runoff (Keenan et al., 2013; Massmann et al., 2019; Orth and Destouni, 2018; Rigden et al., 2016; van Der Sleen et al., 2015; Wagle et al., 2015). Vegetation transpiration occupies most of ET amount, so vegetation control effects can greatly alter the variability of land surface ET (Costa et al., 2010; Jaramillo et al., 2018; Wei et al., 2017; Williams et al., 2012). Moreover, human activities including agricultural irrigation and land use management, are constantly altering the exchange of water and heat between terrestrial ecosystems and the atmosphere (Padrón et al., 2020; Teuling et al., 2019). When these effects are taken into account, the semi-empirical equations for estimating ET and traditional drought indices also face challenges (Yang et al., 2020). Existing studies with respect to global surface fluxes inferred from flux tower observations, remote sensing products and reanalysis data, and statistical approaches, e.g., the results estimated by model tree ensemble (MTE), rely on the satellite era and instantaneous meteorological observations (Jung et al., 2010; Jung et al., 2011; Miralles et al.,

2013). Thus, the existing products cannot be used for long-term trends as they cannot represent the long-term effects of confounders such as CO_2 or species composition changes. This is why we use an opposite view – we use in essence a boundary layer budget based on Salvucci and Gentine (2015) and Gentine et al. (2016) except that we lump the non-linearity for the boundary layer budget in a neural network. Indeed, the diurnal cycle of temperature is directly related to the sensible heat flux. Similarly, the course of specific humidity related to the rate of latent heat flux (Gentine et al., 2011). If there are changes in latent heat flux due to stomatal closure to higher CO_2, this is still captured by the change in the specific humidity in the boundary layer. Moreover, the existing products are based on data that are highly localized, especially in the northern hemisphere. The network of weather station is both much longer but also extend to many locations such as in the tropics, providing much more constrain in those places, where other retrievals typically display very large uncertainties. The aim of our strategy in this study is therefore to infer a longer surface fluxes as well as better generalization to the tropics and other remote regions.

In this study, we propose a new strategy for estimating latent heat flux (λE) (ET in energy units) and sensible heat flux (H) based on observation-driven and machine learning approach. This strategy utilizes daily observations of meteorological variables such as temperatures, humidity, and solar radiation (Salvucci and Gentine 2015; Gentine et al., 2016). A major advantage is that the retrieval process is purely driven by routine weather station observations; therefore, it does not rely on any assumptions on the land processes (e.g., biomass, species composition or CO_2 level), and it can represent the effects of long-term changes in land-surface conditions. Moreover, the observational record of the weather station network is not only longer, but also extends to more remote places, such as the tropics. Thus, the strategy provided in this study allows the monitoring of long-term changes in λE and H with accounting for shifting environmental conditions and better generalizes to tropical regions and other remote areas. To more accurately characterize the changes in surface aridity/wetness, the evaporative fraction (EF), i.e., the ratio of λE to the sum of λE and H, and a proxy for long-term runoff, i.e., the difference of precipitation (P) and ET (P−ET), were employed to quantify the change in aridity/wetness in this study.

2 Observational data and methodology

2.1 Flux tower observational data

We collected the half-hourly/hourly observational data and the integrated daily product from the FLUXNET2015 FULLSET dataset (Pastorello et al., 2020). To control the quality of the observational dataset, this study only used measurements and good-quality gap-filled data from 212 globally distributed flux towers (Supplementary Fig. S1a). The flux towers used in this study across various climate regions and land cover types (Fig. 1). The longest period of data availability is 22 years. This study intended to build a machine learning model for retrieving latent heat and sensible heat fluxes on a daily scale. Therefore, daily-scale data of top-of-atmosphere shortwave radiation, vapor pressure deficit (VPD), mean temperature, and surface wind speed were collected from the integrated daily product. VPD was used to calculate relative humidity. Daily

maximum and minimum temperatures were obtained from the half-hourly/hourly flux tower measurement data. Moreover, daily-scale λE and H were also collected from the integrated daily product. The underlying surfaces of the flux towers covered different plant function types (PFTs). According to the classification scheme of International Geosphere-Biosphere Programme, the PFTs include Croplands (CRO), Deciduous Needleleaf Forests (DNF), Evergreen Needleleaf Forest (ENF),

100   Evergreen Broadleaf Forest (EBF), Deciduous Broadleaf Forest (DBF), Mixed Forest (MF), Grasslands (GRA), Savannas (SAV), Woody Savannas (WSA), Closed Shrublands (CSH), Open Shrublands (OSH), Wetlands (WET), and Snow and Ice (SNO). These flux tower observation data across different ecosystems are used to train and build machine learning model for the retrieval of latent heat and sensible heat fluxes.
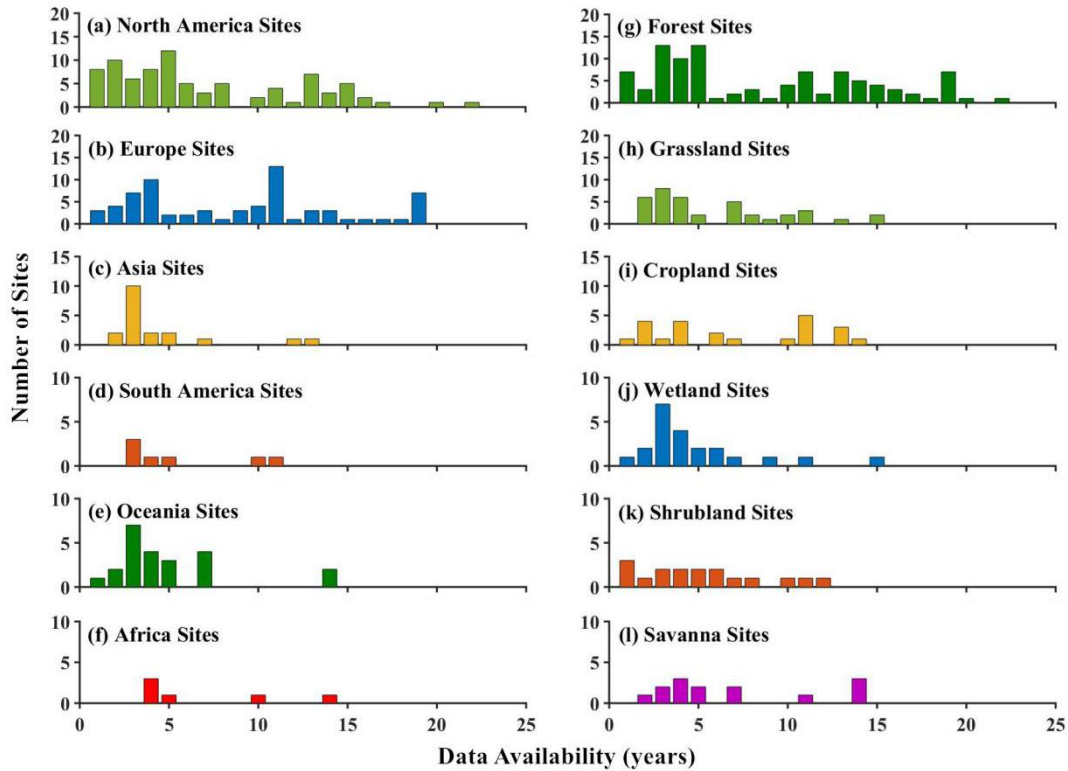
105   **Figure 1.** Data summary of the flux towers used in this study.

2.2 Weather station observation data

Daily observational records of precipitation (P), temperature (mean, maximum, and minimum temperatures), dew point temperature, and wind speed at weather stations were collected from the Global Summary of the Day (GSOD) during the 1950–2017 period. Dew point temperature data were used to calculate the relative humidity, and the daily weather station

110   data on the global land were used to drive a well-trained machine learning model to retrieve long-term water and heat fluxes. The quality of the data was controlled through several procedures (Durre et al., 2010; Matsuura et al., 2009; Yin et al., 2018).

First, we divided the weather stations into two groups: the original stations and the target stations. We used 20 048 sites in total as the original station group (Supplementary Fig. S1b). The target station group was obtained according to the following steps: (1) The stations with a time series spanning less than ten years in length were excluded; (2) if the stations had the same geographic coordinates, we used the stations with a long observation record to replace the stations with a short observation record; (3) if there were multiple stations having different coordinates in a 0.1-degree grid, we removed the stations with a short observation record. After filtering, the target station group which were determined to be used to estimate long-term trends were obtained.

Other procedures for controlling data quality were also implemented. Any implausible values, such as negative precipitation or a maximum temperature lower than the minimum temperature, were excluded. Monthly mean, maximum, and minimum temperatures, as well as monthly precipitation were derived from daily observational data at the original stations. Considering the large uncertainty in the observational data of precipitation, we also compiled the daily precipitation records with precipitation records in another archives, i.e., the Global Historical Climatology Network (GHCN-Daily). The daily records of all weather stations that had the same coordinates as the GHCN-Daily in the GSOD were compared, and the missing daily records were supplemented using the GHCN-Daily archives. Monthly precipitation, temperatures (mean, maximum, and minimum temperatures), relative humidity, and surface wind speed were calculated when the number of missing days within a month was no more than seven days. Additionally, missing monthly data from the target stations were spatially interpolated from the original weather stations using the Kriging method in ArcGIS platform.

2.3 Top-of-atmosphere shortwave radiation model

Solar shortwave radiation is a key factor affecting surface energy and water cycle. Since there is no reliable long-term surface observational solar radiation data, top-of-atmosphere shortwave radiation was used as a replacement. Cloud effects are inherently captured by the diurnal cycle of temperature and humidity (Gentine et al., 2013a,b). Daily top-of-atmosphere shortwave radiation converted from the hourly top-of-atmosphere shortwave radiation was forced to drive the ANN model for predicting the daily λE (H) at the target weather stations. The amount of incoming shortwave radiation at any location/time at the top of atmosphere is a function of Earth–Sun geometry, which is defined as: i) latitude (i.e., location); ii) hour of day (due to the rotation of the earth); and iii) day of year (due to the tilted axis of the earth and its elliptical orbit around the sun). Several models for the top-of-atmosphere fluxes based on these inputs are available at varying levels of precision. The time-location model (Margulis, 2017) used in this study is shown as follows.

$$R_{s0} = \begin{cases} I_0 \dfrac{\cos\theta_0}{d^2}, & daytime : |\theta_0| \le 90° \\ 0, & nighttime \end{cases} \qquad (1)$$

where the cosine of the solar zenith angle is as follows:

$$\cos\theta_0 = \sin\delta\sin\lambda + \cos\delta\cos\lambda\cos\tau \qquad (2)$$

$$\delta = \frac{23.45\pi}{180} \cos\left[\frac{2\pi}{365}(172 - DOY)\right] \quad (3)$$

$$\tau = 2\pi \frac{T_h - 12}{24} \quad (4)$$

145

$$d = 1 + 0.017 \cos\left[\frac{2\pi}{365}(186 - DOY)\right] \quad (5)$$

Here, θ_0 is the solar zenith angle, δ is the declination angle, λ is latitude, τ is the hour angle, DOY represents the day of year, d represents the distance between the sun and Earth normalized by the mean distance, and T_h represents solar hour of the day.

2.4 Artificial neural network model training

150 The artificial neural networks (ANN) have been shown to be powerful non-linear regressions tools. Pure ANN models have good performance in retrieving surface fluxes, and even in some cases, its performance is better than the hybrid model (Chen et al., 2020; Haughton et al., 2018; Zhao et al., 2019). In this study, we trained a multi-layer feedforward neural network model that consisted of an input layer, hidden layers, and an output layer to predict daily λE and H at the globally distributed weather stations. To identify the sensitivities of latent heat and sensible heat fluxes to different variables in the retrieval,

155 ANN model was tested using different variable combinations as input (Supplementary Table S1). Top-of-atmosphere shortwave radiation, relative humidity, surface wind speed, and the mean, maximum, and minimum temperatures were determined to be the inputs of the neural network (Supplementary Table S2).

In the process of training ANN model, input data were randomly divided into three subsets using the percentages of 80%,

160 10%, and 10% for training, validation, and testing, respectively. The mean squared error (MSE) was used to evaluate the performance of the neural network in the training process of adjusting weight. The root mean squared error (RMSE) and pearson correlation coefficient (R) between the ANN predicted λE (H) and the observed λE (H) in the validation set were used to evaluate the retrieval performance of the trained ANN model. A neural network with 2 hidden layers can achieve the same performance as with a large number of hidden layers, so we used the lowest complexity model and enhanced its

165 nonlinear ability by adding neurons. As for the optimal number of neurons, we initially tested it according to an empirical formula, i.e., $h = \sqrt{(n+m)} + a$ (n is the number of input neurons, m is the number of output neurons, and a is a constant ranging from 0 to 10). The neural network was determined to have two hidden layers and 15 neurons per hidden layer, and the ANN model showed good performance and appropriate training time (Supplementary Fig. S2). A tangent sigmoid transfer function was used in the hidden layers, and a linear transfer function was used in the output layer. To avoid over-

170 fitting, the early stopping method was used, that is, we recorded the best validation accuracy during the training process, and the training was stopped when the MSE was no longer reduced after going through additional epochs. The maximum number

of training epochs and training accuracy goal were set to 500 epochs and 0.0001, respectively. Once one of the parameters exceeded the set threshold, the model training was stopped.

2.5 EF linked to surface resistance (r_s) and aerodynamic resistance (r_a)

175   Here, we show that a long-term decline in EF can be strongly impacted by an increase in surface resistance (r_s). The latent heat flux ($L_v E$) is expressed by the following formula.

$$L_v E = L_v \rho \frac{e_{sat}(T_s) - e_a}{r_a + r_s} \tag{6}$$

where L_v is the latent heat of vaporization, E is evaporation flux, ρ is air density, T_s is near-surface air temperature, $e_{sat}(T_s)$ is saturated vapor pressure at the surface, e_a is actual air vapor pressure, r_a is aerodynamic resistance, and r_s is

180   surface resistance. EF can be expressed as follows.

$$EF = \frac{L_v E}{L_v E + H} = \frac{L_v \rho \dfrac{e_{sat}(T_s) - e_a}{r_a + r_s}}{L_v \rho \dfrac{e_{sat}(T_s) - e_a}{r_a + r_s} + H} \tag{7}$$

We used the linearized Clausius–Clapeyron relation (Eq. (8) and Eq. (9)) to simplify Eq. (7).

$$e_{sat}(T_s) = e_{sat}(T_a) + \Delta(T_s - T_a) \tag{8}$$

$$T_s - T_a = \frac{H}{\rho c_p} \tag{9}$$

185   where T_a is the air temperature, $e_{sat}(T_a)$ is saturated vapor pressure of the air, and $\Delta = \dfrac{L_v}{R_v} \dfrac{e_s}{T^2}$, R_v is the gas constant for water vapor. Furthermore, c_p is the specific heat capacity, which is 4216 J kg^{-1} K^{-1} when the temperature is 0 °C.

$$EF = \frac{\dfrac{L_v \rho}{r_a + r_s}((e_{sat}(T_a) - e_a)) + \dfrac{\Delta H}{\rho c_p}}{\dfrac{L_v \rho}{r_a + r_s}((e_{sat}(T_a) - e_a)) + H} \tag{10}$$

$$= \frac{\dfrac{L_v \rho}{r_a + r_s}\left\{VPD + \dfrac{\Delta H}{\rho c_p}\right\}}{\dfrac{L_v \rho}{r_a + r_s}\left\{VPD + \dfrac{\Delta H}{\rho c_p}\right\} + H} \tag{11}$$

$$= \cfrac{1}{1+\cfrac{r_a+r_s}{L_v\rho(\cfrac{\Delta}{\rho c_p}+\cfrac{VPD}{H})}} \tag{12}$$

190   The incremental variation of $\dfrac{VPD}{H}$ is small because both variations of VPD and H are proportional to the temperature variation. EF can be expressed as follows:

$$\frac{1}{EF}=1+\cfrac{r_a+r_s}{\cfrac{L_v}{c_p}\Delta} \tag{13}$$

Hence, r_s is a function of EF.

$$r_s=\frac{L_v}{c_p}\Delta(\frac{1}{EF}-1)-r_a \tag{14}$$

195   Therefore, EF is closely connected with surface resistance and aerodynamic resistance. A decline in EF can be induced by an increase in surface resistance. Annual EF ranges from 0 to 1, and r_a is a function of wind speed with a relatively small variations while the variations in r_s can be strong.

3 Results and discussion

3.1 ANN model retrievals

200   Cross-validations of the ANN model were performed in terms of the values and trends of λE (H). We randomized samples of 10 randomly chosen flux towers from different PFTs as the validation set, and then used the remaining samples to train the ANN model. The ANN predicted daily λE (H) values of the validation set were compared with their observed values (Fig. 2a). The correlation coefficient (R) between the predicted daily λE and the observed daily λE is 0.849 and the R between the predicted daily H and the observed daily H is 0.743, and both correlations are significant at the p<0.001 level. Furthermore,
205   cross-validations were performed for different PFTs. The samples of the validation set were randomly from one PFT (Supplementary Fig. S3). The abilities of the trained ANN model for predicting latent heat and sensible heat fluxes were different for various PFTs. With the exception of OSH (R=0.680, p<0.05), the R of the daily λE of DBF, MF, SAV, GRA, CRO, and WET were all greater than 0.80, and all correlations were statistically significant at the p<0.001 level. A common feature of these land covers is that they belong to the ecosystems with relatively open water bodies or high vegetation
210   coverage, while the OSH is mixed with vegetation and bare soil and thus the vegetation coverage is highly heterogeneous. Therefore, the correlation coefficient at OSH was relatively low, but the correlation was also significant at the p<0.05 level. With respect to the daily H, the correlation coefficients for all PFTs were greater than 0.716 with the exception of R for CRO

(R=0.656, p<0.05), and all were statistically significant at the p<0.001 level. In addition, the trained ANN model also shows good simulation ability under some other ecosystems with relatively sparse vegetation cover such as savannas (SAV), grasslands (GRA), croplands (CRO), and wetlands (WET) (Supplementary Fig. S4). In summary, in addition to OSH, the accuracy of retrieving λE is relatively high in GRA, CRO, WET, and various forest ecosystems, and these ecosystems were characterized by sufficient water supply or dense vegetation cover. For the estimation of H, except for the estimation of H in GRA, the correlations of predicted and observed H in all ecosystems are correlated at the p<0.001 level, especially in forest ecosystems. It needs to be emphasized that the magnitude of R could be affected by the number of samples, and the sample numbers of each verification set in those cross-validations are large (n>12 000). As for the prediction of trends in latent heat and sensible heat fluxes, the ANN model also shows good performance (Fig. 2b). All correlation coefficients between the estimated λE (H) trends and observed λE (H) trends exceeded 0.90 (p<0.001) on ENF, DBF, GRA, and WET, and the correlations on MF, OSH, and CRO exceeded 0.80 (p<0.001), and the correlations surpassed 0.70 (p<0.001) on EBF and SAV (Supplementary Fig. S5 and Fig. S6). In most causes, the accuracy of λE (H) trend estimations using the ANN model are higher than the accuracy of individual λE (H) value estimations.
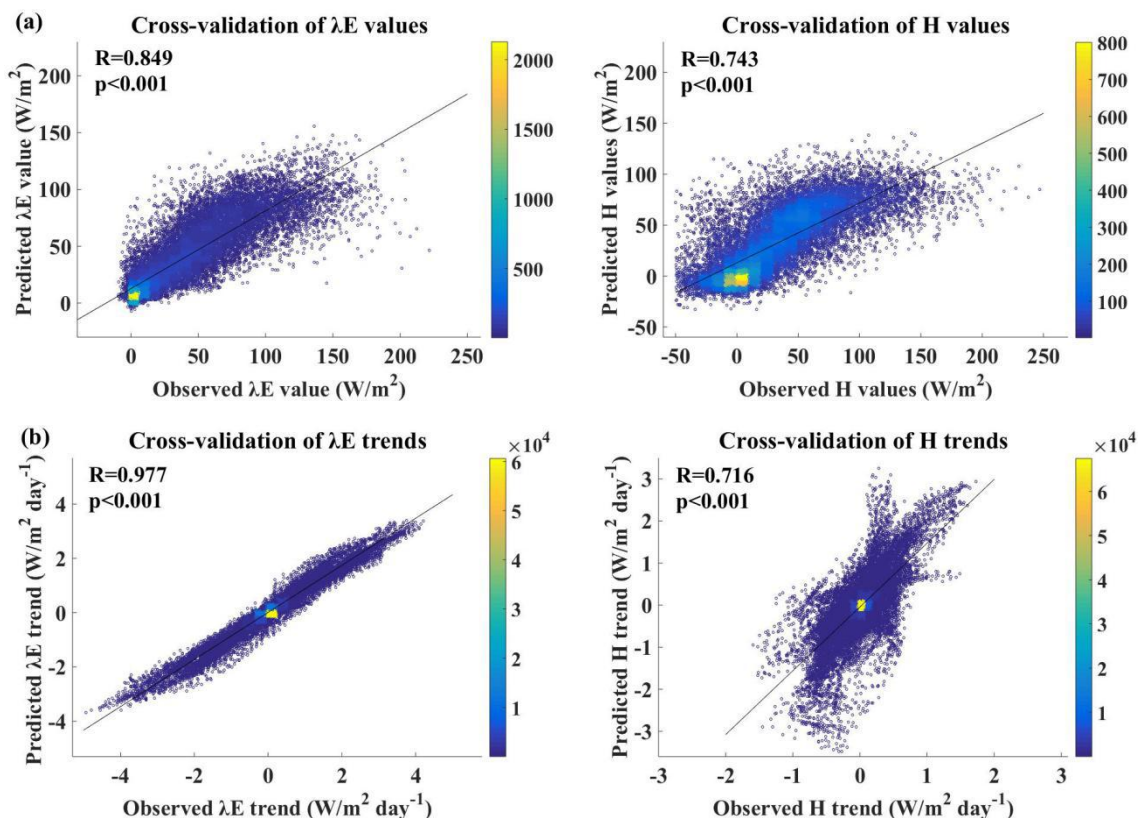

Figure 2. Density scatter plot for (a) the cross-validation in terms of values and (b) the cross-validation in terms of trends. The validation set of values cross-validation is composed of 10 flux towers randomly selected from different plant function types, and the validation set of trends cross-validation is composed of the trends calculated from all time periods.

230 　The uncertainty and bias characteristics of the ANN model retrievals were further analyzed on both daily and monthly scales. At the daily time scale, the RMSE of λE (H) ranged from 26.05 to 26.32 W m^{-2} (28.61 to 29.15 W m^{-2}), and more than 80% of the 212 flux towers had a correlation greater than 0.70. As for the RMSE, 85% and 89% of the daily λE (H) were less than 30 W m^{-2}, respectively (Supplementary Fig. S7). It was obvious that flux towers with large biases were mainly located on the coast of Australia and the west coast and Great Lakes region of the United States, as well as the Mediterranean region, all of

235 which are strongly impacted by advection from neighboring open water bodies. The biases of the monthly λE (H) estimate were smaller than the biases of the daily λE (H) estimate. More than 89% and 90% of the sites had an R greater than 0.70 (Supplementary Fig. S8). Meanwhile, the λE estimation at more than 88% of the sites and the H estimation at more than 89% of the sites showed an RMSE less than 30 W m^{-2}. Similar to the spatial distribution of biases on daily scale, the flux towers with large biases were located on the coast of Australia, the Great Lakes region, and the Mediterranean region. Finally, the

240 daily λE and H of all weather stations over the past few decades were predicted by the trained ANN model. The spatial distribution patterns of mean annual λE and H are consistent with the results predicted by the MTE model, which is a machine learning model for upscaling land surface fluxes from FLUXNET measurements (Jung et al., 2011) (Supplementary Fig. S9). This ensemble of statistical estimates of λE were obtained from the Department of Biogeochemical Integration (BGI) of the Max Planck Institute (MPI) (https://www.bgc-jena.mpg.de/geodb/projects/Data.php). The mean annual ET of

245 the MET model ranged from 0 to 1400 mm (Jung et al., 2010), while the mean annual ET of this study ranged from 0 to 1416 mm during the 1982−2008 period (Supplementary Fig. S10). In different large-scale latitude intervals, the temporal changes of the ANN model estimated λE and the temporal changes of the MET model estimated λE are significantly correlated at the p<0.05 level, which further emphasizes the reliability of the ANN model retrieval results (Supplementary Fig. S11). This study primarily concerned with the direction and magnitude of long-term trends, and thus relative bias can be

250 tolerated.

3.2 Attribution of trends in climate variables

　The trends in climate variables were estimated for two reasons: (1) to quantify the changes in the atmospheric water supply, and (2) to estimate the trends in VPD, air temperature, and surface wind speed to understand the characteristics of changes in

255 atmospheric evaporative demand. The annual precipitation exhibited an increasing trend ranging from 3 to 40 mm per decade in western Europe, the United States, Southeast Asia, and Australia. Conversely, the annual precipitation exhibited a decreasing trend ranging from -3 to -30 mm per decade in northern Eurasia, the savanna region of Brazil, and South Africa (Fig. 3a). In particular, annual precipitation showed a more obvious upward trend than before in a large area of land in recent period, i.e., 2001–2017 (Supplementary Fig. S12). Rising air temperature and the increased water holding capacity of the

260 atmosphere were the primary causes for the substantial increase in precipitation (Byrne et al., 2015), except for some regions (e.g., Russia) with insufficient moisture advection from an ocean or regional evaporation.
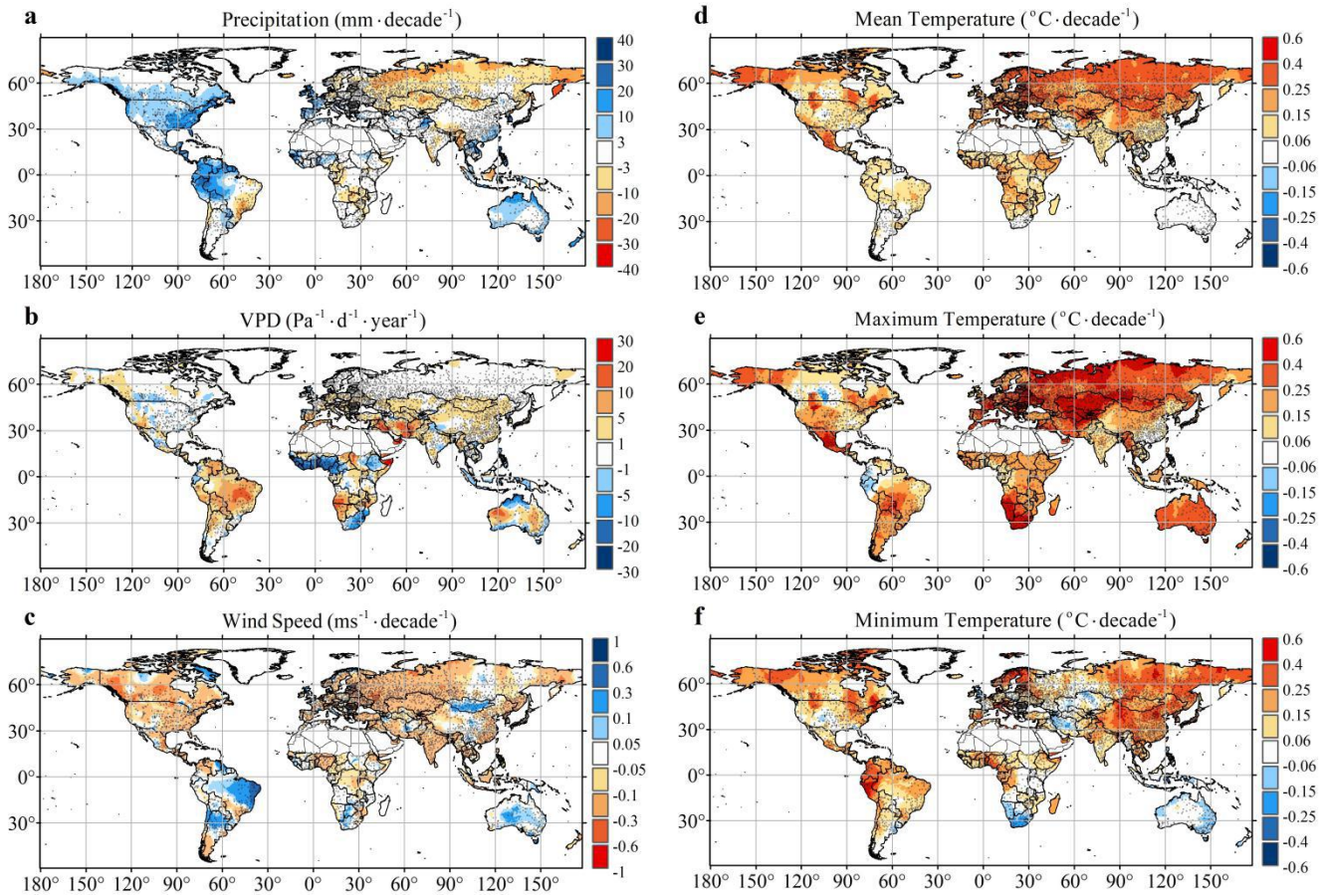
Figure 3. Long-term trends in annual precipitation, vapor pressure deficit (VPD), surface wind speed, mean temperature, maximum temperature, and minimum temperature. Values are not shown for Greenland or Sahara Desert as there are scarce weather station observational data. Small gray squares show locations of the weather stations used to interpolate global patterns.

With respect to the atmospheric water demand sides, the VPD primarily presented an increasing trend because of an increase in air temperature and a decrease in relative humidity, especially in the subtropics (Fig. 3b); this was consistent with the expectations of atmospheric dynamics and the influence of free-tropospheric warming (Held and Soden, 2006). Additional meteorological variables influencing the evaporative demand, such as the mean, maximum, and minimum temperatures, mostly presented increasing trends on the global scale, with the exception of a few areas, such as the United States/Canadian Corn Belt, and Mexico, which showed signs of cooling due to land use management such as agricultural irrigation (Thiery et al., 2017) (Fig. 3d−f). Therefore, both rising air temperatures and increased VPD indicate that the driving forces of soil evaporation and plant transpiration are increasing under the climate warming trend. In addition, the mean surface wind

11

speed—a meteorologic factor associated with evaporation—showed an overall decreasing trend (i.e., global stilling) except in the Amazon, Argentina, Australia, and Mongolia (Fig. 3c).

3.3 Long-term trends in EF, ET, and P–ET

The annual EF ranges from 0 (full aridity stress) to 1 (no aridity stress), and it is an indicator of surface aridity linked to soil moisture availability and vegetation phenology, as well as the physiological effects of atmospheric CO_2 concentrations on vegetation (Francesco et al., 2014; Lemordant et al., 2018; Swann et al., 2016). The decreasing trend in the EF varied from 0 to 0.05 per decade and was prevalent in several land areas (Fig. 4a), except in the most humid areas of tropical rainforest (e.g., the Amazon, West Africa, New Guinea Island, and Southeast Asia) and dense agricultural irrigation areas, including central North America and Punjab in India (Supplementary Fig. S13). Changes in the EF at different latitudinal intervals were consistent with the "dry gets drier, wet gets wetter" paradigm in the tropical areas (Chou et al., 2009; Liu et al., 2013). Moreover, the observed increase in EF further suggested a wet trend in the western Sahel, where an increase in rainfall was reported recently (Biasutti, 2019; Dong et al., 2015). It was systematically determined that the EF declined across large swaths of the globe and exhibited different spatial patterns in different periods of the past few decades, which emphasizeed that this is not a short-term phenomenon (Fig. 5a–c). As the climate has warmed, a decrease in the EF reflected an increase in surface resistance (see Methodology), which can be controlled by one of two factors—either an increase in stomatal resistance associated with the physiological effects of CO_2 or a decrease in soil moisture. Therefore, if we find that soil moisture or surface runoff increases while EF decreases, it is a sign of increased surface resistance impacting the water balance.

The evolution of El Niño–Southern Oscillation (ENSO) can greatly influence the global hydrological cycle and patterns of aridity/wetness (Fu et al., 2012; Miralles et al., 2013; Nalley et al., 2019), and thus we analyzed the patterns of EF in different ENSO phases based on the multivariate ENSO index (MEI). However, no significant changes in EF trends were detected between different ENSO phases, with the exception of La Niña having a significant impact on the aridity in East Asia (Fig. 5d–f). In addition, the EF simulated using an ensemble from Phase 5 of the Coupled Model Intercomparison Project (CMIP5) under the future Representative Concentration Pathway (RCP) 8.5 scenario (the warming scenario with the highest CO_2 emissions) also presented a decreasing trend in most global land areas, even if the trend in the CMIP5 model appeared to be stronger than that of the trend estimated by the data-driven EF (Fig. 6a). Although the trend magnitudes vary across different periods, we can determine whether the direction of EF decline is a long-term existing phenomenon in historical periods and simulated future scenarios. The Earth System Model simulation results further suggested that the increasing CO_2 concentrations can affect the allocation of surface energy fluxes and may cause a decrease in EF on large land surface areas. However, the climate model missed several areas where agricultural practices led to an increase in EF, as well as in the tropical rainforest where there was a deviation in peak precipitation (Yin et al., 2013).

12

As the climate warmed, ET showed a significant upward trend ranging from 0 to 0.03 mm per day per year (Fig. 4b), especially in the core regions of tropical rainforests (e.g., the Amazon, West Africa, and Southeast Asia), the coast of Australia, and the areas with a high density of agricultural irrigation (e.g., northern India, Central Asia, and Central America). The increase in ET was primarily induced by the radiative effect of a warming climate, which can compensate for the observed decrease trend in EF ($ET = EF \times R_n$). Moreover, the observation-driven results showed a declining trend in ET at a rate of 0 to -0.03 mm per day per year on fractional land surfaces, such as North America, South Africa, Australia, Southeast Asia, and the Mediterranean region, which was consistent with the ET declining trends simulated by the CMIP5 climate models for the RCP8.5 scenario (Fig. 6b).
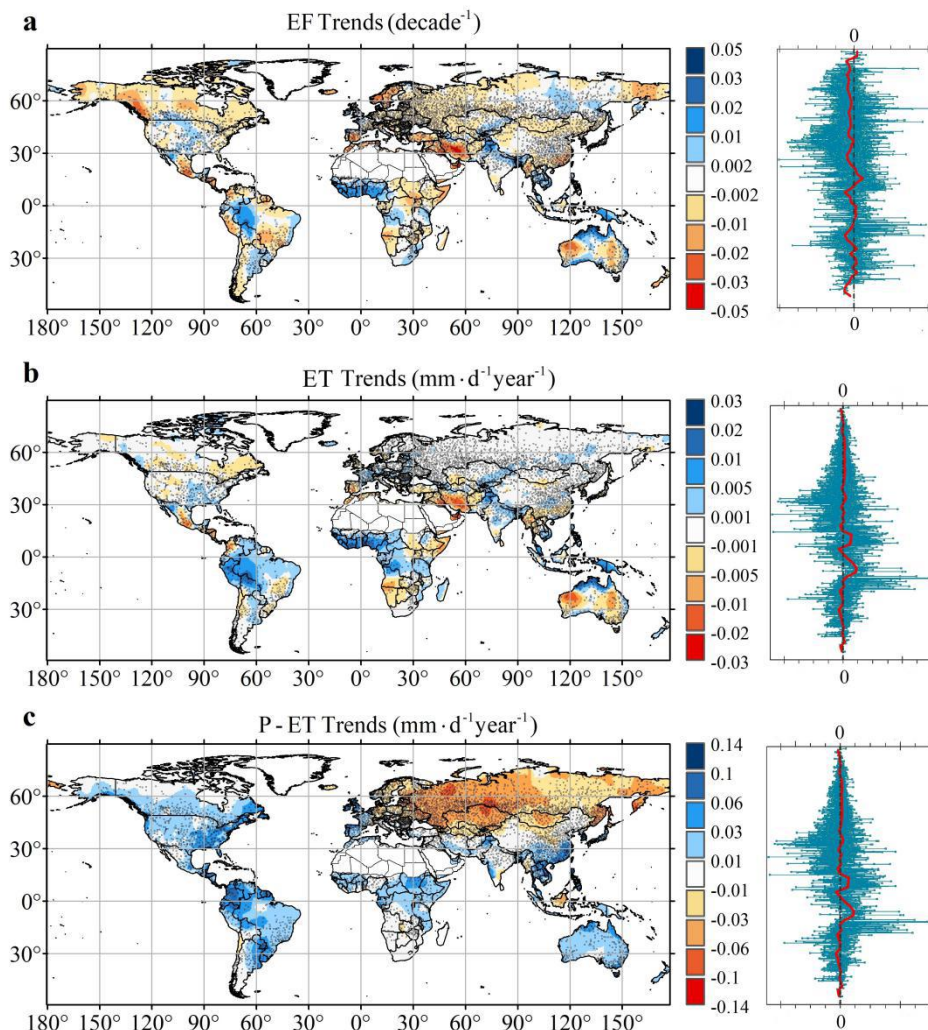
Figure 4. Long-term trends in evaporative fraction (EF), evapotranspiration (ET), and precipitation (P) minus ET (P−ET). ET was converted from the ANN retrieved latent heat flux. The red curve represents median trends at different latitudes.
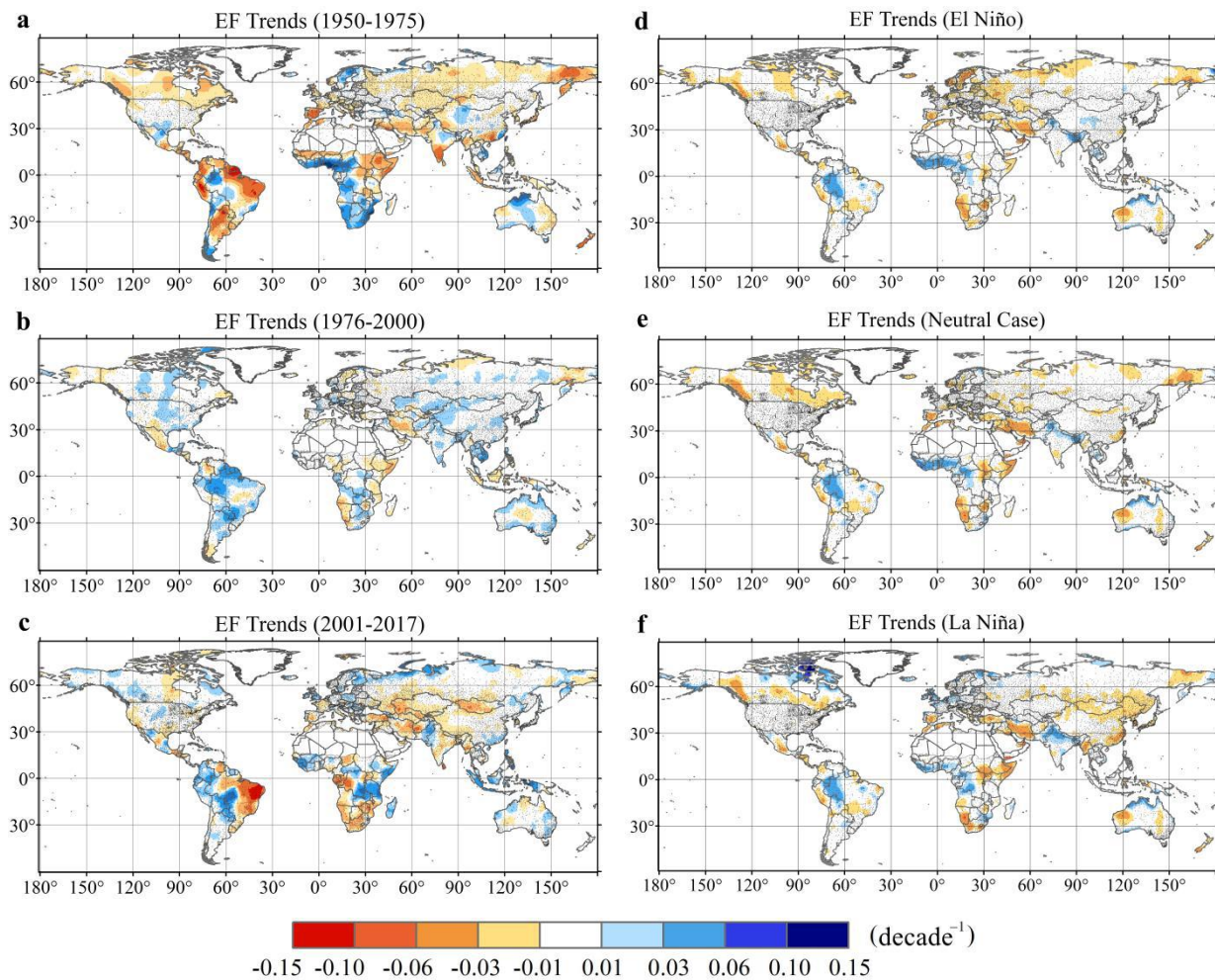
Figure 5. Spatial patterns of EF trends during different periods. (a–c) The spatial patterns show EF trends during different historical periods, and (d–f) the spatial patterns show EF trends during El Niño period, a neutral case period, and La Niña period, respectively.

P−ET, a proxy for long-term runoff, assumes that changes in storage due to human activity are negligible and are closely linked to water availability and soil moisture trends (Alkama et al., 2013; Sophocleous et al., 2002). Therefore, long-term runoff mainly presented an increasing trend on most of the global land, with the exception of a decrease in northern Eurasia (Fig. 4c). To further verify the retrieved P−ET trend, we compared the P−ET trend with the observed streamflow trend during the same periods in small- and medium-sized watersheds (5~1000 km^2) (Supplementary Fig. S14). The P–ET and observed streamflow presented different trends in eastern Australia, which can be attributed to a decrease in runoff caused by human activities as there are clusters of cities in this area (Bosmans et al., 2017). We should not fully expect the P-ET to be completely consistent with observed streamflow, because in addition to measurement errors, the observed streamflow is

14

330　strongly affected by human activities especially on long time scales. Nevertheless, similarities were also found between the P–ET trends and the observed streamflow trends. In western Europe and eastern North America, both P–ET and observed streamflow showed an increasing trend, and in the Mediterranean region and South Africa, both trends showed a decreasing trend. The CMIP5 models under RCP8.5 also predicted an overall increasing trend in P−ET (Fig. 6c), while a decrease was predicted (but it has not been observed) in the western United States and western Europe. Additionally, P−ET was predicted

335　to increase in northern Eurasia, but it has not been widely observed.
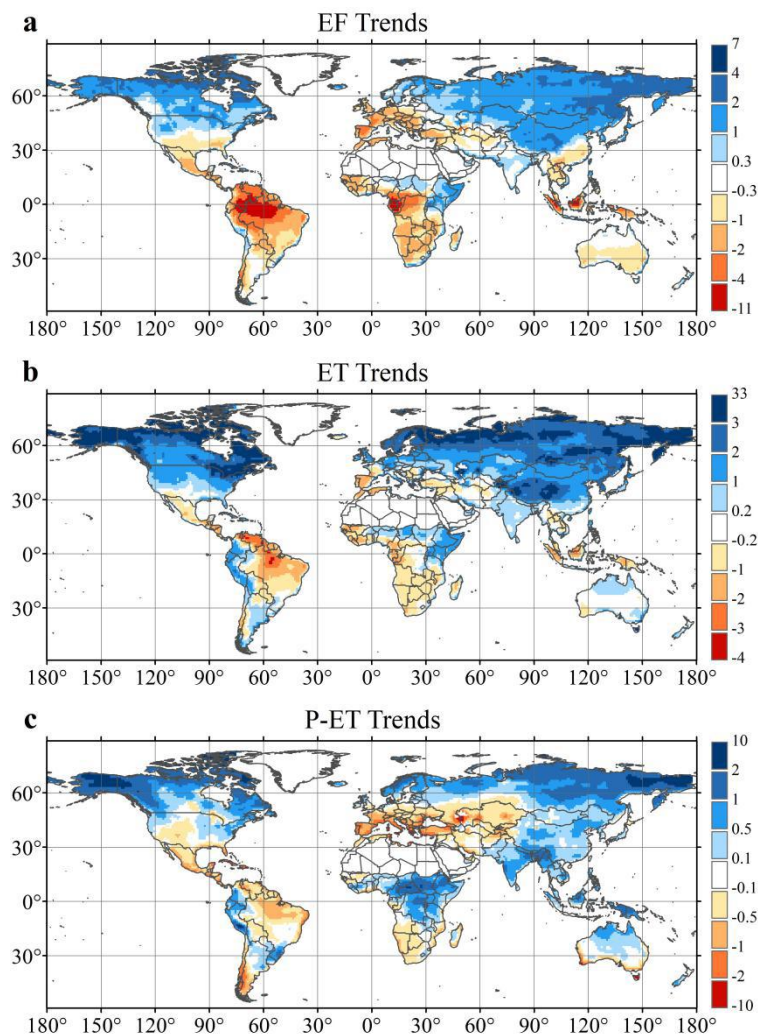
Figure 6. Annual changes in (a) EF, (b) ET, and (c) P−ET in Phase 5 of the Coupled Model Intercomparison Project (CMIP5) under the RCP8.5 scenario with all anthropogenic forcing (e.g., land use/land cover changes, aerosols, and ozone). Changes are quantified by difference in years 2070−2099 of simulation and years 1941−1970.

340

15

3.4 Signs of covariations in long-term EF and runoff

The signs of covariation in normalized ET, i.e., EF, and normalized P−ET, i.e., 1−ET/P, were further investigated to determine the patterns of surface aridity. We superimposed the EF trend, indicative of changes in aridity stress (e.g., temperature and soil moisture) or plant physiological effects (see Methodology), and the 1−ET/P trend, which was indicative of changes in long-term runoff. Land areas with a decreased EF and an increased 1−ET/P were indicative of a dominance of CO_2 plant physiological effects, because a long-term decline in ET with increasing runoff mainly attributable to surface vegetation control. A decline in the EF caused by a decrease in surface conductance can be offset by an increase in the EF caused by the effects of climate warming. Nevertheless, in 27.06% of the global land areas, the EF has declined and has been accompanied by an increase in long-term runoff, which has been observed in most of North America, parts of South America, the Mediterranean, Africa, Australia, and Southeast China (Fig. 7). These signals further emphasized that surface vegetation controls and its response to changing environment have a great influence on water cycle and surface aridity variability.
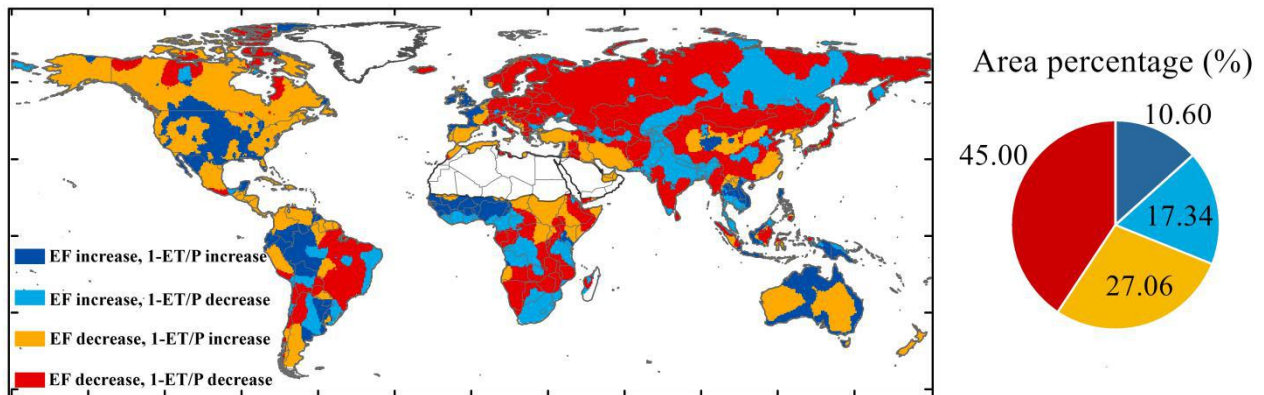

Figure 7. Signs of covariation in EF and 1−ET/P. Right panel shows area percentage of different signs, and the area fractions are calculated by the spherical area.

In addition, the signs of increase in EF with decreasing runoff accounted for 17.34% of the global land areas, which was mainly due to agricultural irrigation and land use management, such as in the Punjab region of India, Central Asia, and downstream Amazon where there is a high density of irrigation (Supplementary Fig. S13). The land areas showing increase trend in both EF and runoff were typically located in humid regions and accounted for 10.60% of the global land surface. With the increase of EF and 1−ET/P, the humid areas of the Amazon, West Africa, Southeast Asia, and the coast of Australia are getting wetter (Fig. 7). Particularly, the previously reported wet trend in western Sahel was captured by the increase trends in both EF and 1−ET/P. Additionally, 45.00% of the global land areas experienced a decreasing trend in EF and 1−ET/P, and thus aridity stress posed a relatively larger risk to these regions. EF and 1−ET/P both exhibited a decreasing trend in the arid regions of the Amazon (e.g., the savanna region of Brazil), and thus those areas are getting drier. Moreover,

365   the Mediterranean region, northern Eurasia, and South Africa also experienced a decrease trend in EF and 1–ET/P, which was consistent with existing observed or predicted results (Padrón et al., 2020; Samaniego et al., 2018; Zhou et al., 2019).

4 Concluding Remarks

This study provides the first strategy for retrieving consistent latent heat and sensible heat fluxes on a global scale over many decades, based on boundary layer budget perspective and using machine learning approach driven by the ground

370   observations of globally distributed flux towers and weather stations. After that, we quantified the attributions of long-term changes in surface aridity/wetness. The results had important implications for understanding variability of land surface aridity under changing environment and provided constraints for future climate model predictions. Although we attempted to infer latent heat and sensible heat fluxes from in situ ground observations and used various data quality control methods to reduce uncertainty, the quality of the observational data from the flux towers and weather stations can influence the

375   retrievals.

In the absence of surface regulation of plant physiological effect and changes in biomass, a warming climate was expected to intensify ET at a rate roughly governed by the Clausius–Clapeyron relation. However, a long-term relative decrease in normalized ET accompanied by increasing runoff was found in 27.06% of the global land areas, which was indicative of a

380   reduction in surface conductance. The findings further emphasized that vegetation controls have strong impacts in regulating the water cycle and surface aridity variability. Climate models have captured some of these changes; however, they have also exhibited large regional discrepancies. Therefore, representations of land use management and plant physiological effects are essential for the improvement of future predictions with respect to the water, energy, and carbon cycles.

385

Author contributions. RW and PG designed the study. RW performed the experiment and wrote the manuscript. PG designed the methodology, analyzed the results, and revised the manuscript. JY and LC contributed to data collection and validation.

395   JC and LL contributed to discussion and supervision.

References

Alkama, R., Marchand, L., Ribes, A., and Decharme, B.: Detection of global runoff changes: results from observations and
CMIP5 experiments. Hydrol. Earth Syst. Sci., 17, 2967–2979, https://doi.org/10.5194/hess-17-2967-2013, 2013.

Baruga, C. K., Kim, D., and Choi, M.: A national-scale drought assessment in Uganda based on evapotranspiration deficits
from the Bouchet hypothesis. J. Hydrol., 580, 124348, https://doi.org/10.1016/j.jhydrol.2019.124348, 2020.

Berg, A., Findell, K., Lintner, B., Giannini, A., Seneviratne, S. I., van den Hurk, B., Lorenz, R., Pitman, A., Hagemann, S.,
Meier, A., Cheruy, F., Ducharne, A., Malyshev, S., and Milly, P. C. D.: Land-atmosphere feedbacks amplify aridity
increase over land under global warming. Nat. Clim. Change, 6, 869–874, https://doi.org/10.1038/nclimate3029, 2016.

Biasutti, M.: Rainfall trends in the African Sahel: Characteristics, processes, and causes. WIREs Clim. Change, 10, e591,
https://doi.org/10.1002/wcc.591, 2019.

Bosmans, J. H. C., van Beek L. P. H., Sutanudjaja, E. H., and Bierkens M. F. P.: Hydrological impacts of global land cover
change and human water use. Hydrol. Earth Syst. Sci., 21, 5603–5626, https://doi.org/10.5194/hess-21-5603-2017,
2017.

Byrne, M. P. and O'Gorman, P. A.: The response of precipitation minus evapotranspiration to climate warming: Why the
"wet-get-wetter, dry-get-drier" scaling does not hold over land. J. Clim., 28, 8078–8092, https://doi.org/10.1175/JCLI-
D-15-0369.1, 2015.

Chen, Z. J., Zhu, Z. C., Jiang, H., and Sun S. J.: Estimating daily reference evapotranspiration based on limited
meteorological data using deep learning and classical machine learning methods. J. Hydrol., 591, 125286,
https://doi.org/10.1016/j.jhydrol.2020.125286, 2020.

Chou, C., Neelin, J. D., Chen, C. A., and Tu, J. Y.: Evaluating the "rich-get-richer" mechanism in tropical precipitation
change under global warming. J. Clim., 22, 1982–2005, https://doi.org/10.1175/2008JCLI2471.1, 2009.

Cook, B. I., Smerdon, J. E., Seager, R., and Coats, S.: Global warming and 21st century drying. Clim. Dyn., 43, 2607–2627,
https://doi.org/10.1007/s00382-014-2075-y, 2014.

Costa, M. H., Biajoli, M. C., Sanches, L., Malhado, A. C. M., Hutyra, L. R., da Rocha, H. R., Aguiar, R. G., and de Araújo,
A. C.: Atmospheric versus vegetation controls of Amazonian tropical rain forest evapotranspiration: Are the wet and

seasonally dry rain forests any different?, J. Geophys. Res.: Biogeo., 115, G04021, https://doi.org/10.1029/2009jg001179, 2010.

Dai, A.: Increasing drought under global warming in observations and models. Nat. Clim. Change, 3, 171–171, https://doi.org/10.1038/nclimate1633, 2013.

435 Durre, I., Menne, M. J., Gleason, B. E., Houston, T. G., and Vose, R. S.: Comprehensive automated quality assurance of daily surface observations. J. Appl. Meteorol. Clim., 49, 1615–1633, https://doi.org/10.1175/2010JAMC2375.1, 2010.

Dong, B. and Sutton, R.: Dominant role of greenhouse-gas forcing in the recovery of Sahel rainfall. Nat. Clim. Change, 5, 757–760, https://doi.org/10.1038/nclimate2664, 2015.

Forzieri, G., Miralles, D., Ciais, P., Alkama, R., Ryu, Y., Duveiller, G., Zhang, K., Robertson, E., Kautz, M., Martens, B.,
440 Jiang, C., Arneth, A., Georgievski, G., Li, W., Ceccherini, G., Anthoni, P., Lawrence, P., Wiltshire, A., Pongratz, J., Piao, S., Sitch, S., Goll, D. S., Arora, V. K., Lienert, S., Lombardozzi, D., Kato, E., Nabel, J. E. M. S., Tian, H., Friedlingstein, P., and Cescatti, A.: Increased control of vegetation on global terrestrial energy fluxes. Nat. Clim. Change, 10, 356–362, https://doi.org/10.1038/s41558-020-0717-0, 2020.

Fu, C., James, A.L., and Wachowiak, M.P. Analyzing the combined influence of solar activity and El Niño on streamflow
445 across southern Canada. Water Resour. Res., 48, W05507. https://doi.org/10.1029/2011WR011507, 2012.

Fu, Q. and Feng, S.: Responses of terrestrial aridity to global warming. J. Geophys. Res.: Atmos. 119, 7863–7875, https://doi.org/10.1002/2014JD021608, 2014.

Francesco, N., Mirco, B., Gabriele, C., Stefano, B., and Pietro, B.: Evaporative fraction as an indicator of moisture condition and water stress status in semi-arid range land ecosystems. Remote Sens., 6, 6300–6323,
450 https://doi.org/10.3390/rs6076300, 2014.

Gentine, P., Entekhabi, D., and Polcher, J.: The diurnal behavior of evaporative fraction in the soil-vegetation-atmospheric boundary layer continuum. J. Hydrometeorol., 12, 1530–1546, https://doi.org/10.1175/2011JHM1261.1, 2011.

Gentine, P., Chhang, A., Rigden, A., and Salvucci, G.: Evaporation estimates using weather station data and boundary layer theory. Geophys. Res. Lett., 43, 11661–11670, https://doi.org/10.1002/2016GL070819, 2016.

455 Gentine, P., Holtslag, A.A., D'Andrea, F. and Ek, M. Surface and atmospheric controls on the onset of moist convection over land. Journal of Hydrometeorology, 14(5), 1443-1462., 2013a.

Gentine, P., Ferguson, C.R. and Holtslag, A.A., Diagnosing evaporative fraction over land from boundary-layer clouds. Journal of Geophysical Research: Atmospheres, 118(15), 8185-8196, 2013b.

Greve, P., Orlowsky, B., Mueller, B., Sheffield, J., Reichstein, M., and Seneviratne, S. I.: Global assessment of trends in
460 wetting and drying over land. Nat. Geosci., 7, 716–721, https://doi.org/10.1038/ngeo2247, 2014.

Held, I. M. and Soden, B. J. Robust Responses of the Hydrological Cycle to Global Warming. J. Clim., 19, 5686–5699, https://doi.org/10.1175/JCLI3990.1, 2006.

Hoek van Dijke, A. J., Mallick, K., Schlerf, M., Machwitz, M., Herold, M., and Teuling, A. J. Examining the link between vegetation leaf area and land–atmosphere exchange of water, energy and carbon fluxes using FLUXNET data. Hydrol. Earth Syst. Sci., 17, 4443–4457, https://doi.org/10.5194/bg-17-4443-2020, 2020.

Jaramillo, F., Cory, N., Arheimer, B., Laudon, H., van der Velde, Y., Hasper, T. B., Teutschbein, C., and Uddling, J: Dominant effect of increasing forest biomass on evapotranspiration: interpretations of movement in Budyko space. Hydrol. Earth Syst. Sci., 22, 567–580, https://doi.org/10.5194/hess-22-567-2018, 2018.

Jung, M., Reichstein, M., Ciais, P., Seneviratne, S.I., Goulden, M. L., Bonan, G., Cescatti, A., Chen, J., de Jeu, R., Dolman, A. J., Eugster, W., Gerten, D., Gianelle, D., Gobron, N., Heinke, J., Kimball, J., Law B. E., Montagnani, L., Mu, Q., Mueller, B., Oleson, K., Papale, D., Richardson, A. D., Roupsard, O., Running, S., Tomelleri, E., Viovy, N., Weber, U., Williams, C., Wood, E., Zaehle, S., and Zhang, K.: Recent decline in the global land evapotranspiration trend due to limited moisture supply. Nat., 467, 951–954, https://doi.org/10.1038/nature09396, 2010.

Jung, M., Reichstein, M., Margolis, H. A., Cescatti, A., Richardson, A. D., Arain, M. A., Arneth, A., Bernhofer, C., Bonal, D., Chen, J., Gianelle, D., Gobron, N., Kiely, G., Kutsch, W., Lasslop, G., Law, B. E., Lindroth, A., Merbold, L., Montagnani, L., Moors, E. J., Pagpale, D., Sottocornola, M., Vaccari, F., and Williams, C.: Global patterns of land-atmosphere fluxes of carbon dioxide, latent heat, and sensible heat derived from eddy covariance, satellite, and meteorological observations. J. Geophys. Res.: Biogeo., 116, G00J07, http://dx.doi.org/10.1029/2010JG001566, 2011.

Keenan, T. F., Hollinger, D. Y., Bohrer, G., Dragoni, D., Munger, J. W., Schmid, H. P., and Richardson, A. D.: Increase in forest water-use efficiency as atmospheric carbon dioxide concentrations rise. Nat., 499, 324–327, https://doi.org/10.1038/nature12291, 2013.

Komatsu, H. and Kume, T.: Modeling of evapotranspiration changes with forest management practices: A genealogical review. J. Hydrol., 585, 124835, https://doi.org/10.1016/j.jhydrol.2020.124835, 2020.

Lemordant, L., Gentine, P., Swann, A. S., Cook, B. I., and Scheff, J.: Critical impact of vegetation physiology on the continental hydrologic cycle in response to increasing CO_2. Proc. Natl. Acad. Sci. USA, 16, 4093–4098, https://doi.org/10.1073/pnas.1720712115, 2018.

Liu, C. and Allan, R. P.: Observed and simulated precipitation responses in wet and dry regions 1850–2100. Environ. Res. Lett., 8, 034002, https://doi.org/10.1088/1748-9326/8/3/034002, 2013.

Mallick, K., Trebs, I., Boegh, E., Giustarini, L., Schlerf, M., Drewry, D. T., Hoffmann, L., Von Randow, C., Kruijt, B., Araùjo, A., Saleska, S., Ehleringer, J. R., Domingues, T. F., Ometto, J. P. H. B., Nobre, A. D., Luiz Leal De Moraes, O., Hayek, M., William Munger, J., and Wofsy, S. C.: Canopy-scale biophysical controls of transpiration and evaporation in the Amazon Basin, Hydrol. Earth Syst. Sci., 20, 4237–4264, https://doi.org/10.5194/hess-204237-2016, 2016.

Margulis, S. A., Introduction to hydrology, 2017. https://margulis-group.github.io/teaching/.

Massmann, A., Gentine, P., and Lin, C.: When does vapor pressure deficit drive or reduce evapotranspiration?. J. Adv. Model. Earth Syst., 11, 3305–3320, https://doi.org/10.1029/2019MS001790, 2019.

Miralles, D. G., DeJeu, R. A. M., Gash, J. H., Holmes, T. R. H., and Dolman, A. J.: Magnitude and variability of land evaporation and its components at the global scale, Hydrol. Earth Syst. Sci., 15, 967–981, https://doi.org/10.5194/hess-15-967-2011, 2011.

Miralles, D. G., Van, d. B. M. J., Gash, J. H., Parinussa, R. M., de Jeu, R. A. M., Beck, H. E., Holmes, T. R. H., Carlos Jiménez, C., Verhoest, N. E. C., Dorigo, W. A., Teuling, A. J., and Dolman, A. J.: El Niño–La Niña cycle and recent trends in continental evaporation. Nat. Clim. Change, 4, 122–126, https://doi.org/10.1038/nclimate2068, 2013.

Miralles, D. G., Brutsaert, W., Dolman, A. J., and Gash, J. H.: On the use of the term "evapotranspiration". Water Resour. Res., 56, e2020WR028055, https://doi.org/10.1029/2020WR028055, 2020.

Milly, P. C. and Dunne, K. A.: Potential evapotranspiration and continental drying. Nat. Clim. Change, 6, 946–949, https://doi.org/10.1038/nclimate3046, 2016.

Nalley, D., Adamowski, J., Biswas, A., Gharabaghi, B., and Hu, W.: A multiscale and multivariate analysis of precipitation and streamflow variability in relation to ENSO, NAO and PDO. J. Hydrol., 574, 288–307, https://doi.org/10.1016/j.jhydrol.2019.04.024, 2019.

Naumann, G., Alfieri, L., Wyser, K., Mentaschi, L., Betts, R. A., Carrao, H., Spinoni, J., Vogt, J., and Feyen, L.: Global changes in drought conditions under different levels of warming. Geophys. Res. Lett., 45, 3285–3296, https://doi.org/10.1002/2017GL076521, 2018.

Ned, H., Gab, A., and Pitman, A. J.: On the predictability of land surface fluxes from meteorological variables. Geosci. Model Dev., 11, 195–212, https://doi.org/10.5194/bg-15-4495-2018, 2018.

Orth, R., and Destouni, G: Drought reduces blue-water fluxes more strongly than green-water fluxes in Europe. Nat. Commun., 9, 3602, http://dx.doi.org/10.1038/s41467-018-06013-7, 2018.

Padrón, R. S., Gudmundsson, L., Decharme, B., Ducharne, A., Lawrence, D. M., Mao, J., Peano, D., Krinner, G., Hyungjun Kim, H., and Seneviratne, S. I.: Observed changes in dry-season water availability attributed to human-induced climate change. Nat. Geosci., 2020, 13(7): 477–481, https://doi.org/10.1038/s41561-020-0594-1, 2020.

Pastorello, G., Trotta, C., Canfora, E., Chu, H., Christianson, D., Frank, J., Massman, W., and Urbanski, S.: The FLUXNET2015 dataset and the ONEFlux processing pipeline for eddy covariance data. Sci. Data, 7, 225, https://doi.org/10.1038/s41597-020-0534-3, 2020.

Rigden, A. J. and Salvucci, G. D.: Evapotranspiration based on equilibrated relative humidity (ETRHEQ): Evaluation over the continental US. Water Resour. Res., 51, 2951–2973, https://doi.org/10.1002/2014WR016072, 2015.

Rigden, A. J. and Salvucci, G. D.: Stomatal response to humidity and CO_2 implicated in recent decline in US evaporation. Global Change Biol., 23, 1140–1150, https://doi.org/10.1111/gcb.13439, 2016.

Salvucci, G. D. and Gentine, P.: Emergent relation between surface vapor conductance and relative humidity profiles yields evaporation rates from weather data. Proc. Natl. Acad. Sci. USA, 110, 6287–6291, https://doi.org/10.1073/pnas.1215844110, 2013.

Samaniego, L., Thober, S., Kumar, R., Wanders, N., Rakovec, O., Pan, M., Zink, M., Sheffield, J., Wood, E. F., and Marx, A.: Anthropogenic warming exacerbates European soil moisture droughts. Nat. Clim. Change, 8, 421–428, https://doi.org/10.1038/s41558-018-0138-5, 2018.

Sheffield, J., Wood, E. F., and Roderick, M. L.: Little change in global drought over the past 60 years. Nat., 491, 435–438, https://doi.org/10.1038/nature11575, 2012.

Sorokin, Y., Jane Zelikova, T., Blumenthal, D., Williams, D. G., and Pendall, E.: Seasonally contrasting responses of evapotranspiration to warming and elevated CO_2 in a semi-arid grassland. Ecohydrol., 10, e1880, https://doi.org/10.1002/eco.1880, 2017.

Sophocleous, M.: Interactions between ground water and surface water: the state of the science. Hydrogeol. J., 10, 348–348, https://doi.org/10.1007/s10040-001-0170-8, 2002.

Swann, A. L., Hoffman, F. M., Koven, C. D., and Randerson, J. T.: Plant responses to increasing CO_2 reduce estimates of climate impacts on drought severity. Proc. Natl. Acad. Sci. USA, 113, 10019–10024, https://doi.org/10.1073/pnas.1604581113, 2016.

Thiery, W., Davin, E. L., Lawrence, D. M., Hirsch, A. L., and Seneviratne, S. I.: Present-day irrigation mitigates heat extremes. J. Geophys. Res.: Atmos., 122, 1403–1422, https://doi.org/10.1002/2016JD025740, 2017.

Trenberth, K. E., Dai, A., Van Der Schrier, G., Jones, P. D., Barichivich, J., Briffa, K. R., and Sheffifield, J.: Global warming and changes in drought. Nat. Clim. Change, 4, 17–22, https://doi.org/10.1038/NCLIMATE2067, 2014.

Teuling, A. J., De Badts, E. A. G., Jansen, F. A., Fuchs, R., Buitink, J., Hoek Van Dijke, A. J., and Sterling, S. M.: Climate change, reforestation/afforestation, and urbanization impacts on evapotranspiration and streamflow in Europe. Hydrol. Earth Syst. Sci., 23, 3631–3652, https://doi.org/10.5194/hess-23-3631-2019, 2019.

Van der Schrier, G., Jones, P. D., and Briffa, K. R.: The sensitivity of the PDSI to the Thornthwaite and Penman-Monteith parameterizations for potential evapotranspiration. J. Geophys. Res.: Atmos. 116, D03106, https://doi.org/10.1029/2010JD015001, 2011.

Vicente-Serrano, S. M., Van Gerard, V. D. S., Beguería, S., Azorin-Molina, C., and Lopez-Moreno, J. I.: Contribution of precipitation and reference evapotranspiration to drought indices under different climates. J. Hydrol., 526, 42–54. http://dx.doi.org/10.1016/j.jhydrol.2014.11.025, 2015.

van der Sleen, P., Groenendijk, P., Vlam, M., Anten, N. P. R., Boom, A., Bongers, F., Pons, T. L., Terburg, G., and Zuidema, P. A.: No growth stimulation of tropical trees by 150 years of CO_2 fertilization but water-use efficiency increased. Nat. Geoscience, 8, 24–28, https://doi.org/10.1038/NGEO2313, 2015.

Wagle, P., Xiao, X., Scott, R. L., Kolb, T. E., Cook, D. R., Brunsell, N., Baldocchi, D. D., Basara, J., Matamala, R., Zhou, Y., and Bajgain, R.: Biophysical controls on carbon and water vapor fluxes across a grassland climatic gradient in the United States, Agr. Forest Meteorol., 214/215, 293–305, https://doi.org/10.1016/j.agrformet.2015.08.265, 2015.

Williams, C. A., Reichstein, M., Buchmann, N., Baldocchi, D., Beer, C., Schwalm, C., Wohlfahrt, G., Hasler, N., Bernhofer, C., Foken, T., Papale, D., Schymanski, S., and Schaefer, K.: Climate and vegetation controls on the surface water

balance: Synthesis of evapotranspiration measured across a global network of flux towers, Water Resour. Res., 48, W06523, https://doi.org/10.1029/2011WR011586, 2012.

565   Williams, I. N. and Torn, M. S.: Vegetation controls on surface heat flux partitioning, and land-atmosphere coupling, Geophys. Res. Lett., 42, 9416–9424, https://doi.org/10.1002/2015gl066305, 2015.

Wei, Z., Yoshimura, K., Wang, L., Miralles, D. G., Jasechko, S., and Lee, X. H.: Revisiting the contribution of transpiration to global terrestrial evapotranspiration, Geophys. Res. Lett., 44, 2792–2801, https://doi.org/10.1002/2016GL072235, 2017.

570   Yang, Y. T., Roderick, M. L., Zhang, S., McVicar, T. R., and Donohue, R. J.: Hydrologic implications of vegetation response to elevated CO_2 in climate projections. Nat. Clim. Change, 9, 44–48. https://doi.org/10.1038/s41558-018-0361-0, 2019.

Yang, Y. T., Zhang, S. L., Roderick, M. L., McVicar, T. R., Yang, D. W., Liu W. B., and Li X. Y.: Comparing Palmer Drought Severity Index drought assessments using the traditional offline approach with direct climate model outputs.
575   Hydrol. Earth Syst. Sci., 24, 2921–2930. https://doi.org/10.5194/hess-24-2921-2020, 2020.

Yin, J. B., Gentine, P., Zhou, S., Sullivan, S. C., Wang, R., Zhang, Y., and Guo S. L.: Large increase in global storm runoff extremes driven by climate and anthropogenic changes. Nat. Commun., 22, 9, 4389, https://doi.org/10.1038/s41467-018-06765-2, 2018.

Yin, L., Fu, R., Shevliakova, E., and Dickinson, R. E.: How well can CMIP5 simulate precipitation and its controlling
580   processes over tropical south America?. Clim. Dynam., 41, 3127–3143, https://doi.org/10.1007/s00382-012-1582-y, 2013.

Zhao, W. L., Gentine, P., Reichstein, M., Zhang, Y., Zhou, S., Wen, Y., Lin, C., Li, X., and Qiu, G.Y.: Physics-constrained machine learning of evapotranspiration. Geophys. Res. Lett., 46, 14496–14507, https://doi.org/10.1029/2019GL085291, 2019.

585   Zhou, C. and Wang, K.: Biological and environmental controls on evaporative fractions at AmeriFlux sites. J. Appl. Meteorol. Clim., 55, 145–161. https://doi.org/10.1175/JAMC-D-15-0126.1, 2016.

Zhou, S., Williams, A. P., Berg, A. M., Cook, B. I., Zhang, Y., Stefan, H., Ruth, L., Seneviratne, S. I., and Gentine, P.: Land–atmosphere feedbacks exacerbate concurrent soil drought and atmospheric aridity. Proc. Natl. Acad. Sci. USA, 116, 18848–18853, https://doi.org/10.1073/pnas.1904955116, 2019.